Molecular Mechanism of Electrostatic Field-Enhanced Water Vapour Absorption at the Gas-Solution Interface

This is the PREPRINT version of this article. The final, published version of the article can be found at:
https://doi.org/10.1016/j.icheatmasstransfer.2025.109610

Fangsu Fan[a], Yonggao Yin[a,b*], Guoying Xu[a,b], Wanhe Chen[a], Christos N. Markides[c]

[a] *School of Energy and Environment, Southeast University, Nanjing 210096, China*
[b] *Engineering Research Centre of Building equipment, Energy, and Environment, Ministry of Education, China*
[c] *Clean Energy Processes (CEP) Laboratory, Department of Chemical Engineering, Imperial College London, London SW7 2AZ, UK*
[*] *Corresponding author. Email: y.yin@seu.edu.cn*

Abstract: Gas-solution mass transfer is critical in industrial manufacturing, chemical processing, and indoor humidity control. Liquid desiccant dehumidification (LDD) systems offer energy-efficient, environmentally friendly humidity control by utilising low-grade heat and avoiding conventional refrigerants, but their performance is limited by low interfacial vapour absorption. Interfacial transport—absorption, reflection, and release—is governed by structural properties, providing a molecular-level perspective for enhancement. This study proposes active control water vapour transport at the LiBr solution vapour-liquid interface using an external electrostatic field (*E*-field) applied along the mass transfer direction to induce interfacial polarisation. Molecular dynamics (MD) simulations show that the *E*-field increases net absorption, with positive fields more effective than negative ones. Both polarities enhance absorption by reorienting water dipoles, disrupting hydrogen-bond (H-bond) networks, and promoting diffusion. Reflection and release are highly polarity-dependent: positive fields enrich Li^+ at the

interface, strengthening hydration and trapping water, suppressing release; negative fields deplete Li^+ and accumulate Br^-, weakening hydration and facilitating release. These findings provide a molecular framework for enhancing interfacial mass transfer through external field modification to improve dehumidification and may also guide optimisation of other gas-liquid processes involving polar molecules.

Keywords: Vapour-liquid interface; Polarisation effect; Water absorption; Diffusion coefficient; Molecular dynamics simulation.

1. Introduction

Addressing energy security and environmental protection is crucial for global sustainable development. In sectors with high dehumidification demand, such as indoor climate control and industrial manufacturing processes, energy consumption is especially high [1]. This highlights the urgent need for energy-saving and environmentally friendly dehumidification technologies. LDD systems have emerged as an alternative to conventional vapour-compression condensation dehumidification. Driven by the water vapour partial pressure difference between liquid desiccants, such as LiBr and LiCl solution, and humid air [2], LDD systems eliminate the use of high global warming potential (GWP) refrigerants and enable regeneration with low-grade thermal energy sources, including solar energy and industrial waste heat [3,4]. LDD systems have demonstrated significant potential for energy savings and environmental benefits. However, their performance remains constrained by the intrinsically low gas-solution diffusion rate, which constitutes a critical bottleneck limiting further improvements in system efficiency [5,6]. Thus, in-depth investigation of the mechanisms and development of enhancement strategies for interfacial mass transfer are essential for broader application of these systems [7].

The vapour-liquid interface, as the critical region for water molecule absorption and release, exhibits mass transfer behaviours strongly governed by interfacial properties [8,9], as revealed by previous MD simulations, a widely used approach for probing microscopic mechanism [10,11]. Chen et al. [12] reported that ion-water interactions depend on ion type and dipole orientation. Pan et al. [13] found that

variations in molecular dipoles alter interfacial free energy barriers, with lower barriers facilitating water release. Weng et al. [14] observed that the formation of ion clusters at the interface enhances the absorption capacity of LiBr solution. As interfacial properties critically govern water absorption and release, this study proposes regulating interfacial molecular behaviour by manipulating interfacial structures with external fields. The *E*-field was selected as the intervention method due to its effective polarisation of ions and polar molecules [15].

Microscopic studies have been extensively applied in interfacial science and electrochemistry to investigate the effects of *E*-fields on interfacial properties and mass transfer behaviours of solvents and ions. For equilibrium interfacial properties, applying a low- to moderate-strength *E*-field (0.01 V ·nm^{-1} to 10 V ·nm^{-1}) in water-air and electrolyte-air systems induces significant reorientation of water molecules while avoiding electrolysis [16,17]. This effect is largely confined to the gas-liquid interface, with limited influence on the bulk liquid [18]. Our previous simulation study [19] confirmed that the *E*-field effectively polarises the concentrated salt solution-air interface, leading to ion enrichment/depletion and enhanced orientational ordering of water molecules. Wang et al. [20] similarly observed that water molecules in salt solution droplets adopt field-aligned orientation under an applied *E*-field. For mass transfer processes, existing studies have mainly examined the influence of *E*-fields on pure water systems [21–23]. Fei et al. [21] reported a 15.6% increase in the evaporation rate of pure water under an *E*-field, attributing the enhancement to reduced surface free energy. Han et al. [22] demonstrated that under an *E*-field of 0.2 V·nm^{-1}, the diffusion coefficient of ozone in water increased from 1.32×10^{-6} to 1.88×10^{-6} cm^2 s^{-1}, attributing this to reduced surface tension and disruption of hydrogen bonding (H-bond). Liu et al. [23] showed that *E*-field regulation of water permeation in nanochannels accelerates both transport and diffusion. The studies above have examined the effects of *E*-fields on the steady-state interfacial properties of pure water/solution systems, or on mass transfer in pure water systems. However, studies on interfacial mass transfer behaviours during water absorption by salt solutions under the influence of *E*-fields are still lacking. This gap hinders the development of new mechanisms to enhance

interfacial mass transfer in salt solutions via polarity regulation under *E*-fields.

To advance *E*-field methods based on interfacial property regulation of mass transfer, systematic investigations into the polarisation response of interfacial structures and their regulatory effects on water molecule behaviours under applied *E*-fields are urgently required. In this study, we first established a concentrated LiBr solution-air interface absorption system under a constant water vapour flux and applied *E*-fields of different polarities along the mass-transfer direction to conduct non-equilibrium molecular dynamics (NEMD) simulations of the absorption process. Transport events were then identified to quantify interfacial transport behaviours under varying *E*-field polarisation, solution concentration, and temperature. Subsequently, interfacial structural properties were assessed in terms of dipole reorientation and particle redistribution, coupled with interfacial water transport channels (dynamic H-bond networks) and transport rates (dynamic diffusion coefficients). Finally, this approach revealed the mechanisms by which polarisation effects promote or hinder specific transport events, and clarified the competitive or synergistic interactions between *E*-field polarisation and solution properties. This work provides a molecular-level theoretical basis for *E*-field-enhanced dehumidification and establishes a research framework for applying *E*-field interventions in interfacial engineering and mass transfer enhancement.

2. Model and methods

2.1 Molecular configuration and simulation procedure

MD simulations were conducted using LAMMPS package [24]. The molecular configuration (**Fig. 1c**) represents water vapour absorption by the LiBr solution, with the pure water region supplied water vapour that was subsequently absorbed by the salt solution. The system dimensions were 5 nm in the *x*- and *y*-directions and 30 nm in the *z*-direction. Table 1 summarises the number of particles in the system. To minimise artefacts from periodic replicas, the left interface of the solution was designated as the adsorption interface for analysis. The temperature of pure water region (T_w) was maintained at 370 K to ensure a sufficient water vapour supply. The LiBr solution

temperatures (T_s) ranged from 280 K to 320 K, consistent with typical operating conditions in LDD systems [25].

Table 1. Number of particles at varying solute concentrations.

	Pure water film	LiBr solution film			Air		Total molecules
	N_{H_2O}	X_s, wt%	N_{H_2O}	$N_{Li^+} = N_{Br^-}$	N_{N_2}	N_{O_2}	
S_I	2000	40	2000	276	12	4	4568
S_{II}	2000	50	2000	415	12	4	4846
S_{III}	2000	60	2000	622	12	4	5260

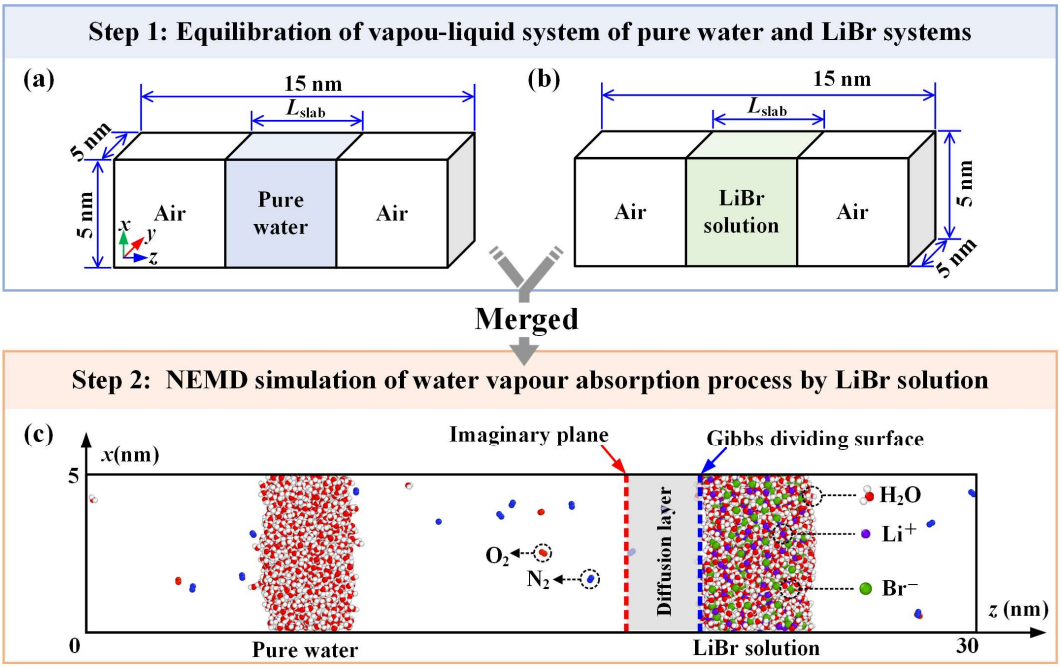


Fig. 1. Molecular configuration of (a) the pure water-air, (b) the LiBr solution-air and the combined (c) absorption systems.

After system equilibration (**Section S1,** Supporting Information), the entire system was relaxed under the NVE ensemble to simulate the absorption process, during which an external *E*-field was applied. Each simulation was performed for 1 ns with a timestep of 0.01 ps, and time-averaged atomic coordinates, velocities, and forces were recorded every 1 ps for analysis. To ensure statistical reliability, ten independent simulations were conducted for each operating condition, with varied initial atomic positions and velocities, while maintaining identical thermodynamic parameters (temperature, pressure, and concentration). The results were averaged to improve the accuracy of the simulation.

2.2 Force field and algorithm for MD simulation

All atoms and ions were treated as charged particles. The total interaction energy between any two particles, U_{tot}, comprises the Lennard-Jones potential (U_{LJ}), and the Coulomb potential (U_{coul}), see **Eqs. (1)** and (**2**). Cross-interaction parameters were determined using the Lorentz-Berthelot mixing rules [26], as defined in **Eq. (3)**.

$$U_{\mathrm{LJ}} = 4\varepsilon_{ij}\left[\left(\frac{\sigma_{ij}}{r_{ij}}\right)^{12} - \left(\frac{\sigma_{ij}}{r_{ij}}\right)^{6}\right] \tag{1}$$

$$U_{\mathrm{coul}} = f\frac{q_i q_j}{r_{ij}} \tag{2}$$

$$\sigma_{ij} = \frac{1}{2}\left(\sigma_i + \sigma_j\right),\ \ \varepsilon_{ij} = \sqrt{\varepsilon_i \cdot \varepsilon_j} \tag{3}$$

where *i* and *j* denote different particles, ε is the potential well depth, σ is the distance at which the potential energy is zero, q is the particle charge, r is the distance between the particle centres, f is the Coulomb's constant with the value of 138.935 $\mathrm{kJ{\cdot}mol^{-1}{\cdot}nm^{-1}{\cdot}e^{-2}}$.

The LJ potential parameters are listed in **Table 2**. The force field parameters for ions were adopted from Koneshan et al. [27], those for air molecules from Frank et al. [28], and the SPC/E [29] model were employed for water. The SHAKE algorithm [30] was employed to constrain the bond lengths and angles of water molecules, removing three degrees of freedom per molecule and leaving six effective degrees of freedom. This correction was applied during temperature control to ensure accurate temperature estimation and reliable thermostat performance. Accordingly, the temperature was calculated using **Eqs. (4)** and (**5**). The LJ potential and short-range electrostatic interactions were truncated at 1.2 nm, while long-range electrostatic interactions were computed using the particle-particle-mesh (PPPM) algorithm [31] with a relative error of 10^{-4}. Newton's equations of motion were solved using the velocity-Verlet algorithm [32], with a 1 fs time step, and periodic boundary conditions are applied in all directions. The reliability of the simulation methods was confirmed through equilibrium checks, size independence tests, and validation against experimental data (**Sections S2-S4**, Supporting Information).

$$T = \frac{2E_{\mathrm{k}}}{k_{\mathrm{B}} \cdot \mathrm{DOF}} \tag{4}$$

$$E_k = \frac{1}{2}\sum_{i=1}^{N} m_i \, v_i^2 \tag{5}$$

where E_{k} is the kinetic energy, k_{B} is the Boltzmann constant, and DOF denotes the degrees of freedom.

Table 2. Potential parameters of atoms.

Atoms/Ions	ε, kcal·mol^{-1}	σ, Å	q, e	r, Å	θ_{HOH}, °
Li^+	0.1649	1.505	1	–	–
Br^-	0.1000	4.539	−1		
O (H_2O)	0.1553	3.166	−0.8476	O-H: 1	109.47
H (H_2O)	0.0000	0.000	0.4238		
N (N_2)	0.1629	3.738	0	N-N: 1.098	–
O (O_2)	0.2038	3.480	0	O-O: 1.017	

2.3 E-field configuration and interfacial characterisation

2.3.1 *E*-field configuration

The *E*-field was applied perpendicular to the solution interface, spanning from 15 nm to 30 nm along the *z*-axis (**Fig. 2**). Within this region, all charged atoms experienced *E*-field forces (see **Eq. (6)**). The corresponding *E*-field potential energy U_{e}, introduced by the *E*-field and added to the total potential energy of the system to account for interactions with the charged atoms, is given in **Eq. (7)**.

$$\mathbf{F} = q_i \cdot \mathbf{E} \tag{6}$$

$$U_{\mathrm{e}} = -\sum_{i=1}^{N} q_i \mathbf{E} \cdot \mathbf{x}_i = -\sum_{i=1}^{N} q_i \left(x_i \cdot E_x + y_i \cdot E_y + z_i \cdot E_z\right) \tag{7}$$

where q_i is the charge of atom i, $\mathbf{E} = (E_x, E_y, E_z)$ is the *E*-field vector with $E_x = E_y = 0$, and $\mathbf{x}_i = (x_i, y_i, z_i)$ denotes the position vector of atom i.

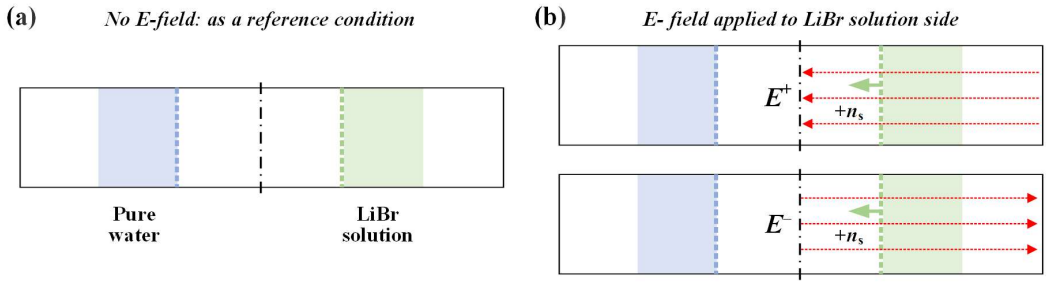


Fig. 2. The *E*-field configuration: (a) no *E*-field and (b) *E*-fields applied to LiBr solution region.

The *E*-field polarity is defined as positive (E^+) when aligned with the positive interfacial normal direction, and negative (E^-) when opposed to it. The interfacial normal is considered positive when pointing from the liquid to the vapour phase. To enhance molecular responses within limited simulation time, stronger *E*-fields than typically used in practical applications (10^5 to 10^6 V·m^{-1}) were employed. In this study, the *E*-field strength ranged from 0.1 V·nm^{-1} to 1 V·nm^{-1}, consistent with typical simulation values and much smaller than the ionisation threshold (10V·nm^{-1}) [20,33]. The absence of *E*-field is denoted as E_0, and a positive *E*-field of 0.5 V·nm^{-1} is denoted as $E_{0.5}^{+}$.

2.3.2 Identification of interfacial molecular behaviours

Identifying molecular migration behaviours, including absorption, release, displacement, and reflection [34], is essential for quantifying the interfacial molecular transport (**Fig. 3a**). These behaviours are determined by the trajectories of water molecules entering the diffusion layer [35,36], defined between the Gibbs dividing surface (GDS) and an imaginary plane located 2 nm from the GDS **(Fig. 1c**). IL_V and IL_L represent the vapour-side and liquid-side interfacial layers, respectively, relative to the GDS (**Fig. 3b**). To accurately locate the diffusion layer, the interfacial layer was defined using the 10-90% criterion [37] corresponding to the region where the density increases from 0.1 to 0.9 of the bulk liquid density. The density profile was obtained by dividing the simulation box along the *z*-axis into 200 slabs, each 0.05 nm thick. The GDS [37] separates the vapor and liquid phase, with its position z_0 determined by fitting the density profile to **Eq. (8)**.

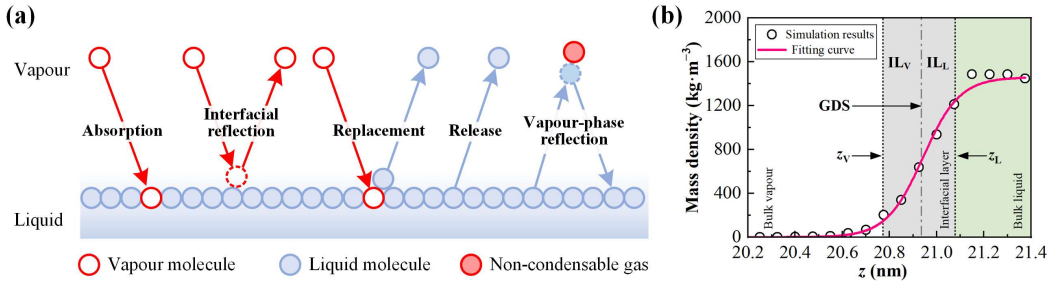


Fig. 3. (a) Diagram of different molecular behaviours and (b) definition of GDS position.

$$\rho(z) = \frac{\rho_l + \rho_v}{2} - \frac{\rho_l - \rho_v}{2} \tanh\left(\frac{z - z_0}{d}\right) \tag{8}$$

where ρ_l and ρ_v are the bulk liquid and bulk vapour densities (kg·m^{-3}), and d is the interfacial layer thickness parameter obtained from the fit.

Molecular migration behaviours are schematically illustrated in **Fig. 3b**. An absorption event occurs when a water vapor molecule from the air crosses the imaginary plane, diffuses through the interfacial layer, enters the solution, transitioning into the liquid phase without inducing phase changes in surrounding water molecules. Reflection occurs when water molecules collide with the interface or other vapour-phase molecules and are redirected back. Interfacial reflection occurs when a water molecule strikes the interface or nearby vapour molecules and is bounced back into the gas phase, reducing the number entering the solution. By contrast, collisions of molecules already in the solution that redirect them within the liquid do not change the net mass transfer. Displacement, describing the simultaneous entry of a water vapour molecule into the solution and expulsion of an adjacent water molecule into the air, was rarely observed [34] and had no effect on the final net absorption. A release event is the reverse of absorption, where water molecules migrate from the solution into the air without inducing phase changes in surrounding water molecules. In this study, the cumulative numbers of the absorption, interfacial reflection, and release events are denoted as N_{abs}, N_{ref}, and N_{rel}, respectively. The net absorption, defined as $N_{net\text{-}abs} = N_{abs} - N_{rel}$, represents the actual number of water molecules migrating from the air into the solution, accounting for both absorption and release events.

2.3.3 Definition of interfacial properties

The orientation of water molecules was characterised by the dipole moment angle θ and the hydroxyl group angles φ_1 and φ_2 (**Fig. 4**). The probability distribution of their projection along the z-axis and the average orientation angle calculated as shown in **Eqs. (9)** and (**10**).

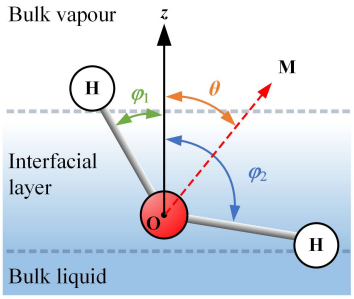


Fig. 4. The definition of water orientation angles.

$$P[cos(\theta_i)] = \frac{cos(\theta_i)}{\sum_{i=1}^{N} cos(\theta_i)} \quad (9)$$

$$\langle\theta\rangle = \sum_{i=1}^{N} \theta_i P\langle\cos(\theta_i)\rangle \quad (10)$$

where θ_i is the dipole angle of the water molecule i (°), and cos(θ_i) represents its projection along the z-axis.

H-bonds were identified using geometric criteria: a donor-hydrogen-acceptor angle $\alpha \leq \alpha_{HB} = 30°$, and a hydrogen-acceptor distance $r \leq r_{HB} = 0.35$ nm. The number of H-bonds per water molecule in each layer was calculated as:

$$N_{HB} = \frac{(2N_{00}+N_{01})}{N_{water}} \quad (11)$$

where N_{00} and N_{01} denote intra- and inter-layer H-bonds, respectively, and N_{water} is the number of water molecules in the layer. H-bonds are inherently dynamic, continuously forming and breaking. Their temporal stability was characterised using the autocorrelation of the H-bond existence function, defined as:

$$C(\tau) = s_i(t) \cdot s_i(t+\tau) \quad (12)$$

$$S_i(t) = \{0, 1\} \quad (13)$$

where $s_i(t) = 1$ indicates the presence of the H-bonds, and $s_i(t) = 0$ indicates its absence. The average H-bond lifetime τ_{HB} was obtained from the integral of the autocorrelation function:

$$\tau_{\mathrm{HB}} = \int_0^{\infty} C(\tau)\mathrm{d}\tau \tag{14}$$

The self-diffusion coefficient (D), reflecting mass transport velocity, was determined from the mean square displacement (MSD) using the Einstein relation (Eq. (15)). In this study, D was calculated every 100 ps, with each value obtained by averaging MSD results over the preceding 100 ps, and one MSD segment extracted every 20 ps.

$$6D = \lim_{t\to\infty} \frac{\mathrm{MSD}(t)}{t} = \lim_{t\to\infty} \frac{\langle|\vec{r}(t)-\vec{r}(0)|^2\rangle}{t} \tag{15}$$

3. Results and discussion

Water molecular transport events were quantified and classified to evaluate the interfacial mass transfer under an applied E-field. During NEMD simulations, the water vapour molecules supply from the pure-water side remained unaffected by changes in solution-side conditions (**Fig. S10**, Supporting Information). As shown in **Fig. 5**, $N_{\text{net-abs}}$ reached 30 over 1 ns under E_0 in a 50 wt% LiBr solution at 280 K, consistent with Chen et al. [34]. The trend followed the order $E_{\perp}^{+} > E_{\perp}^{-} > E_0$, increasing to 36.4 under $E_{0.8}^{+}$ (20.1% increase) and to 35.2 under $E_{0.8}^{-}$ (16.1% increase). A positive field enhanced interfacial absorption while suppressing interfacial reflection and release. In contrast, a negative E-field also increased absorption but simultaneously promoted reflection and release, thereby reducing overall effectiveness.

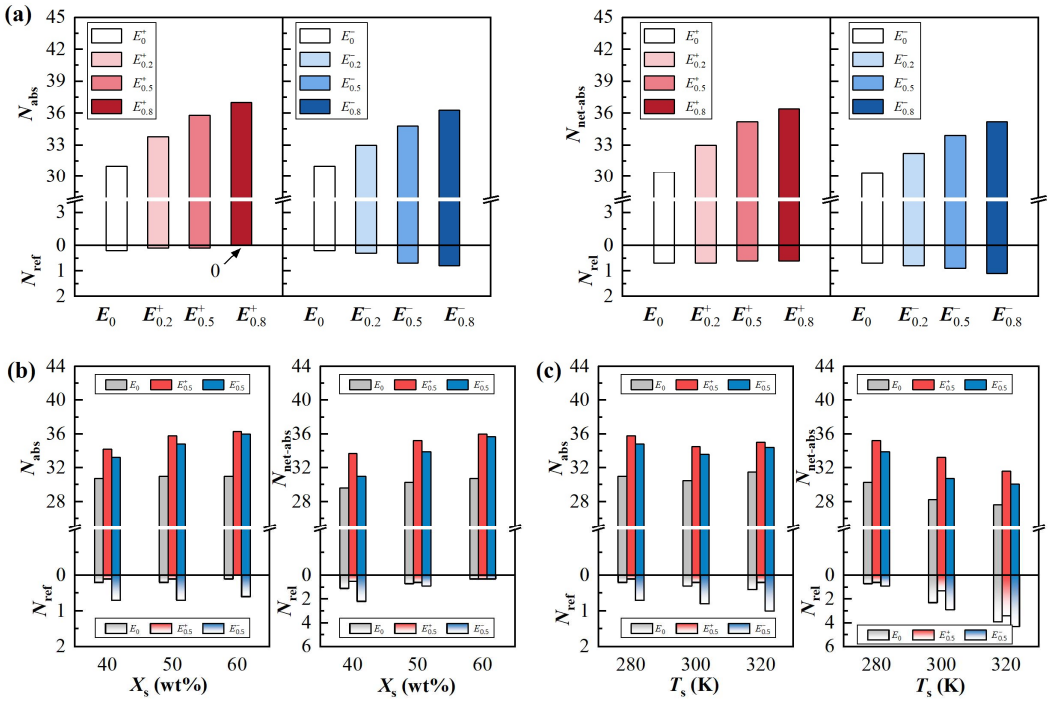


Fig. 5. Effects of the *E*-fields on interfacial molecular behaviours: (a) 50 wt% LiBr, at T_s = 280 K; (b) Varying solution concentrations at fixed T_s = 280 K; (c) Varying solution temperatures at fixed X_s = 50 wt%.

The coupling between X_s, T_s, and *E*-field polarisation effects on interfacial molecular behaviours determines the potential and applicability of *E*-field applications. At lower concentrations and higher temperatures, increased interfacial reflection and release reduce net absorption, as shown in **Fig. 5b**, consistent with previous experimental [38] and molecular [34] observations. A positive field suppresses interfacial reflection and release, whereas the enhanced reflection and release caused by a negative field is detrimental, although net absorption remains elevated within the studied concentration and temperature ranges. The observed differences in interfacial mass transfer behaviours are attributed to *E*-field-induced particle rearrangement and dipole reorientation, with distinct interfacial polarisation responses that either promote or inhibit specific behaviours. The underlying mechanisms will be examined in detail in subsequent sections.

Transport of water molecules across the vapor-liquid interface involves energy transfer. Collisions of water vapour molecules with the solution interface convert part of their kinetic energy into heat (**Fig. 6a**). This is consistent with previous studies

[34,39], which reported temperature rises during condensation or absorption. Consequently, continued water absorption gradually increases the local temperature (**Fig. 6b**), consistent with conventional dehumidification experiments and practical absorption measurements [21]. Under an applied *E*-field, enhanced net absorption slightly elevates the average interfacial temperature (**Fig. 6c**), while the overall thermodynamic state remains essentially unchanged. Quantitative analysis indicates that the total energy varies by –0.18% to 0.59% (**Section S6,** Supporting Information), consistent with DFT results reported by Gao et al. [17].

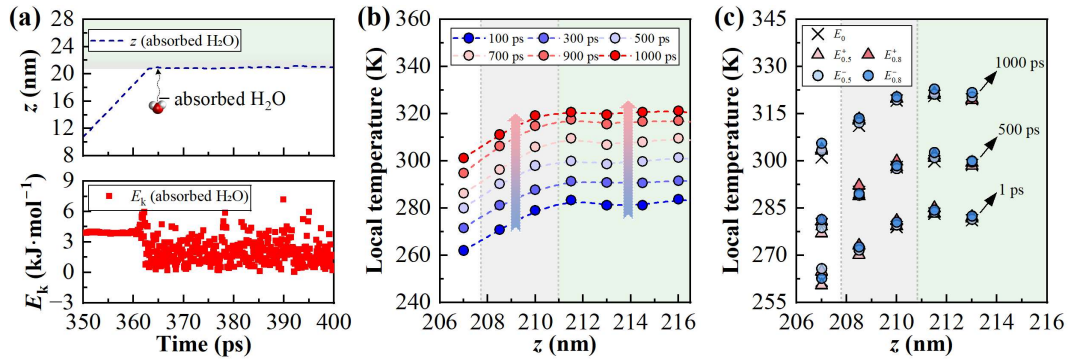


Fig. 6. (a) The trajectory and kinetic energy of a representative absorbed water molecule, (b) local temperature distribution of the solution system and (c) *E*-field induced temperature variation.

Previous studies have shown that water vapour absorption from air is primarily driven by cumulative interactions exerted by particles on the solution side. This driving force depends on the spatial distribution of interfacial particles and is further modulated by the dipole alignment of water vapour molecules [12,37]. Due to the polarising effect of the *E*-field, particle distribution and dipole orientation at the interface are highly sensitive to the applied field [19]. These field-sensitive interfacial structural parameters may act as key drivers of changes in water molecule behaviour. Building on this understanding, we further examined the dynamic evolution of surface water molecule clusters, specifically investigating the effects of the *E*-field on H-bond distribution and lifetimes. As the H-bond network reorganises, intermolecular interactions at the interface are altered, which affects transport pathways and significantly influences the absorption process. Finally, the self-diffusion coefficient of interfacial water molecules was calculated to quantify their mobility near the interface. Collectively, these structural

and dynamic metrics elucidate the molecular mechanisms by which *E*-field-induced polarisation modulates water molecule behaviour at the interface.

During the absorption process, the number of interfacial water molecule increases, triggering further diffusion of ions from the bulk to the interface due to dilution of interfacial solute concentration (**Fig. 7a**).

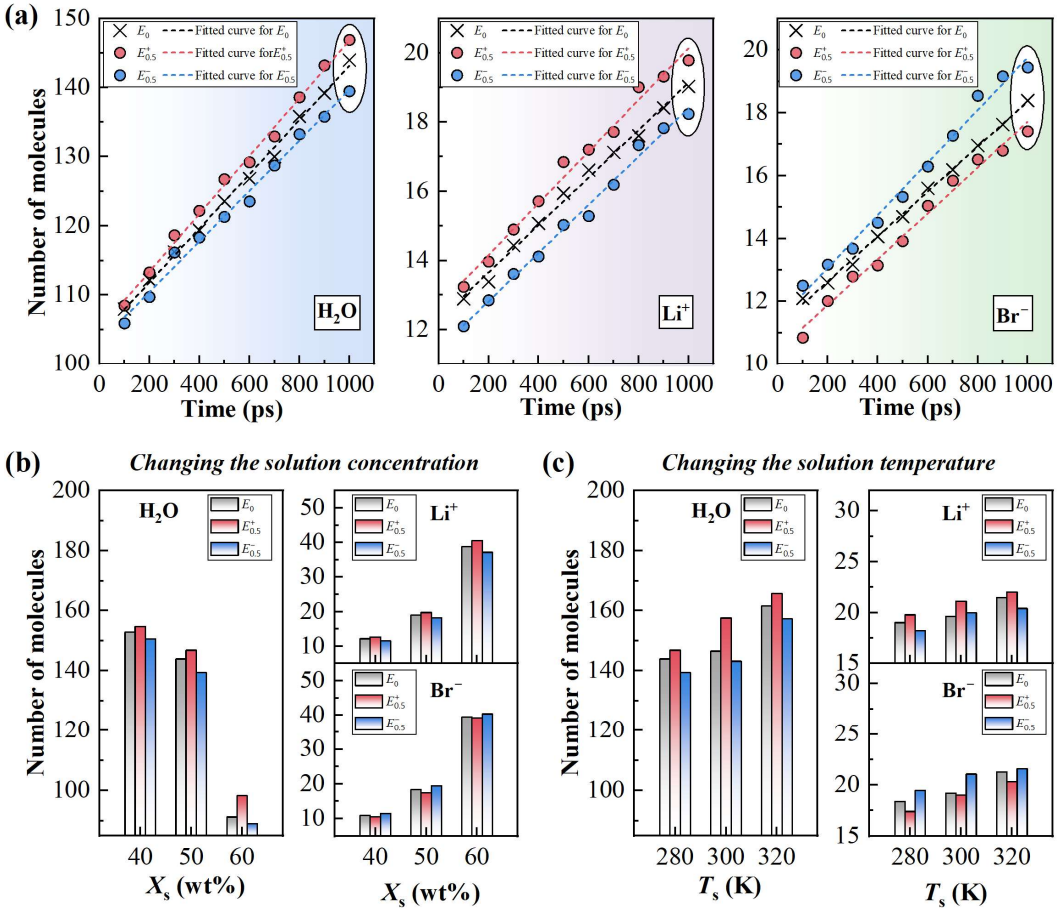


Fig. 7. Effects of *E*-fields on (a) interfacial molecule evolution over time, (b) final interfacial count at (b) different concentrations, and (c) different temperatures.

Higher X_s promotes ion accumulation at the interface, enhancing the capture of neighbouring water molecules (**Fig. 7b**) [40]. Increasing T_s raises the number of water molecules and ions by enhancing thermal motion, which disrupts hydration and expands the interfacial region [41]. Application of the *E*-field induced a rapid response in the distribution of interfacial particles (**Fig. 7**). Under a positive field, Li^+ migrated toward the interface, whereas Br^- moved away due to their opposite charges relative to the field. Consequently, some water molecules are drawn toward the interface by the

strong hydration of Li^+, resulting from its high charge density [42]. Under a negative field, polarisation of Li^+ reduced its interfacial population, whereas Br^- accumulation increases, leading to a decrease in the number of interfacial water molecules. The arrangement of interfacial water molecules depends on ion migration as well as their dipole orientations (**Fig. 8)**.

The reorientation of water dipoles is strongly governed by *E*-field polarity (**Fig. 8**). In contrast to the random distribution of dipole angles in the bulk liquid, interfacial water molecules exhibit orientation peaks below 90°, with an average angle $\langle\theta\rangle = 81°$ over 1 ns, indicating preferential alignment toward the vapour phase [34,43]. This behaviour arises from the lower local density and weaker ion-dipole interactions at the interface, allowing water molecules to respond more readily to the applied *E*-field [19]. Under a positive field, the orientation peak shifts left, and the average angle $\langle\theta\rangle$ decreases by 4.0° (1 ns average), whereas under a negative field, the peak shifts right and $\langle\theta\rangle$ increases by 4.3°, confirming that water dipoles preferentially align with the *E*-field direction. Similar reorientation of hydroxyl angles is shown in **Figs. S12** and **S13** of Supporting Information. This orientational polarisation preference accounts for the polarity-dependent release behaviours shown in **Fig. 5**. Under a positive field, dipoles align towards the vapour side, with oxygen atoms closer to liquid phase and hydrogen toward the vapour phase, facilitating Li^+ hydration and interfacial capture. In contrast, under a negative *E*-field, interfacial Li^+ ions are depleted while Br^- ions accumulate; their weak hydration limits ion-water binding at the interface [18]. Additionally, dipole reorientation positions oxygen atoms away from the liquid phase and hydrogen atoms toward it, forming an interfacial water structure more prone to disruption [44], thereby promoting interfacial water release.

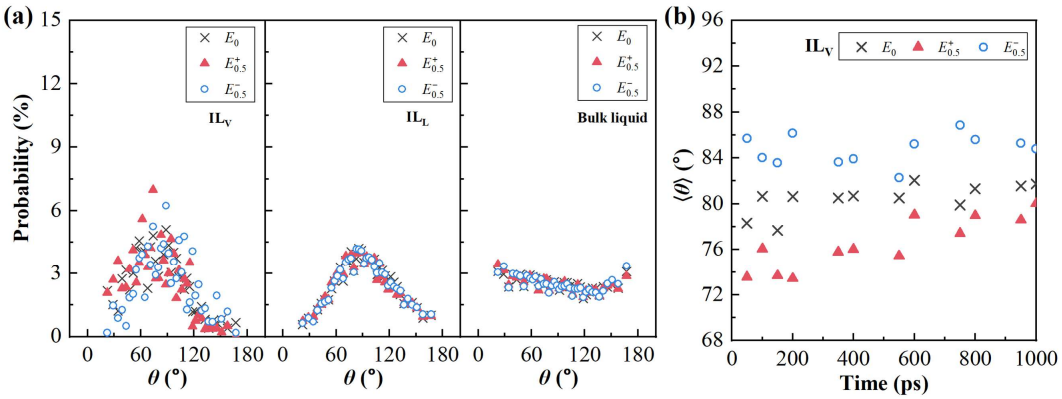


Fig. 8. Effects of *E*-fields on the (a) probability distributions and (b) averaged orientation angles of dipole angle θ of water molecules in different regions.

H-bonds between water molecules form a network that regulates interfacial transport. As shown in **Fig. 9**, under an applied *E*-field, water reorientation disrupts the H-bond network by reducing coordination numbers, an effect amplified at the interface due to molecular asymmetry [43], particularly on the vapour side. Under a positive field, hydrogen atoms orient away from the oxygen atoms in the liquid phase that can act as H-bond acceptors, while enhanced ion enrichment and hydration further intensify H-bond network disruption, making the effect more pronounced than under a negative field [45].

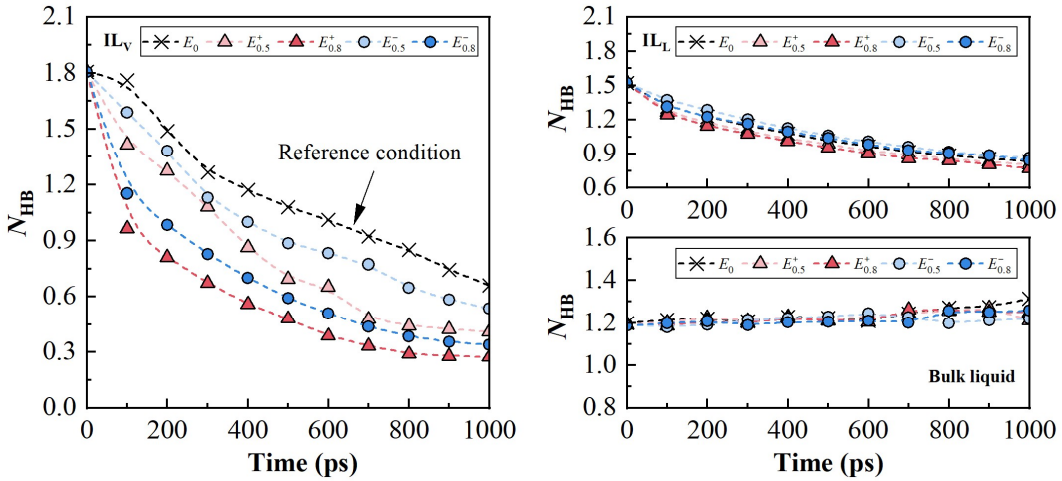


Fig. 9. Effects of the *E*-fields on the number of H-bonds in different layers near surface.

Increased concentration, due to ion effects, and elevated temperature, due to intensified thermal motion, disrupt the H-bond network, while the *E*-field effect on H-bond numbers remains evident (**Fig. S14**, Supporting Information). *E*-fields also

modulate H-bond dynamics, reducing bond lifetimes, as shown in **Fig. 10**, consistent with previous findings [19,46]. A reduced number of H-bonds facilitates water molecules transport across the interfacial layer by lowering intermolecular shear viscosity [23,47]. Variations in microscopic water transport rates are characterised by the self-diffusion coefficient (**Fig. 11**).

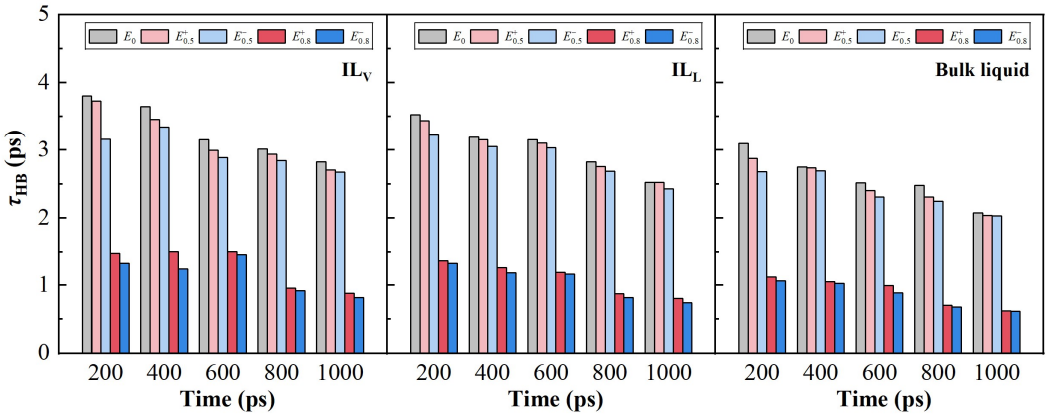


Fig. 10. Effect of the *E*-field on H-bond lifetimes.

Disruption of the H-bond network facilitates the cross-interface migration of water molecules by creating less constrained transport pathways, a phenomenon confirmed by the increased diffusion coefficients (**Fig. 11**). In the vapour-side interfacial layer, the diffusion coefficient is 1.1×10^{-5} cm^2·s^{-1} without an *E*-field, consistent with [27,34], increasing by 22% and 8.6% under $E_{0.8}^{+}$ and $E_{0.8}^{-}$, respectively. In the liquid-side interfacial layer, strong ion-dipole interactions constrain the diffusion coefficient, yielding 0.6195×10^{-5}, 0.68×10^{-5}, and 0.623×10^{-5} cm^2·s^{-1} under E_0, $E_{0.8}^{+}$, and $E_{0.8}^{-}$, respectively. Considering the uncertainty of $\pm 0.03 \times 10^{-5}$ cm^2 ·s^{-1} , these variations are negligible. Similarly, the enhancement of diffusion coefficients under *E*-fields persists across different solution X_s and T_s (**Fig. S15**, Supporting Information). The polarity-dependent differences in diffusion reflect variations in H-bond network disruption, indicating that a positive field accelerates interfacial water diffusion more effectively, particularly for vapour-phase molecules.

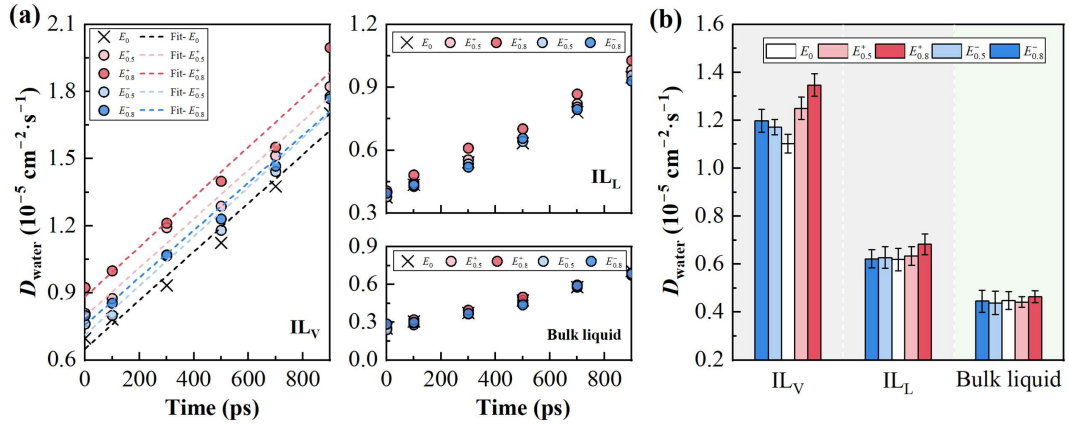


Fig. 11. (a) Self-diffusion coefficient of water molecules and the (b) averaged results within 1 ns.

The *E*-field modulates the structure and dynamics of interfacial water molecules via polarisation, thereby enhancing the moisture absorption performance of liquid desiccants, as illustrated schematically in **Fig. 12**. Under both positive and negative fields, interfacial water molecules undergo polarisation-induced dipole reorientation (**Fig. 8**), weakening H-bond coordination (**Fig. 9**), accelerating network dissociation (**Fig. 10**), opening transport pathways, and enhancing molecular mobility and diffusivity (**Fig. 11**), thereby increasing the probability of absorption events (**Fig. 5**). Positive and negative fields exert distinct, polarity-dependent effects on interfacial water release and reflection. Under a positive field, accumulation of interfacial Li^+ ions (**Fig. 7**) strengthens ion-hydration interactions at the interface, thereby suppressing release and reflection and reinforcing this effect. In contrast, a negative field depletes interfacial Li^+ ions and enriches Br^- ions. Additionally, dipole reorientation positions oxygen atoms away from the liquid phase, weakening hydration and thereby facilitating interfacial water release.

This mechanism demonstrates that external *E*-fields can precisely control ion distribution and dipole orientation, thereby modulating H-bond dynamics and molecular diffusion pathways, enhancing dehumidification efficiency and interfacial mass transfer. These findings provide a molecular-level framework for interface engineering to improve dehumidification performance through interfacial regulation, and can be extended to other external fields or micro/nano-structured surfaces capable of quantitatively controlling interfacial dipoles and ion distributions. Furthermore, these insights may guide the optimisation of other gas-liquid absorption processes

involving polar molecules, such as desalination, CO_2 capture, and hydrogen storage, highlighting their broad potential in interfacial engineering.

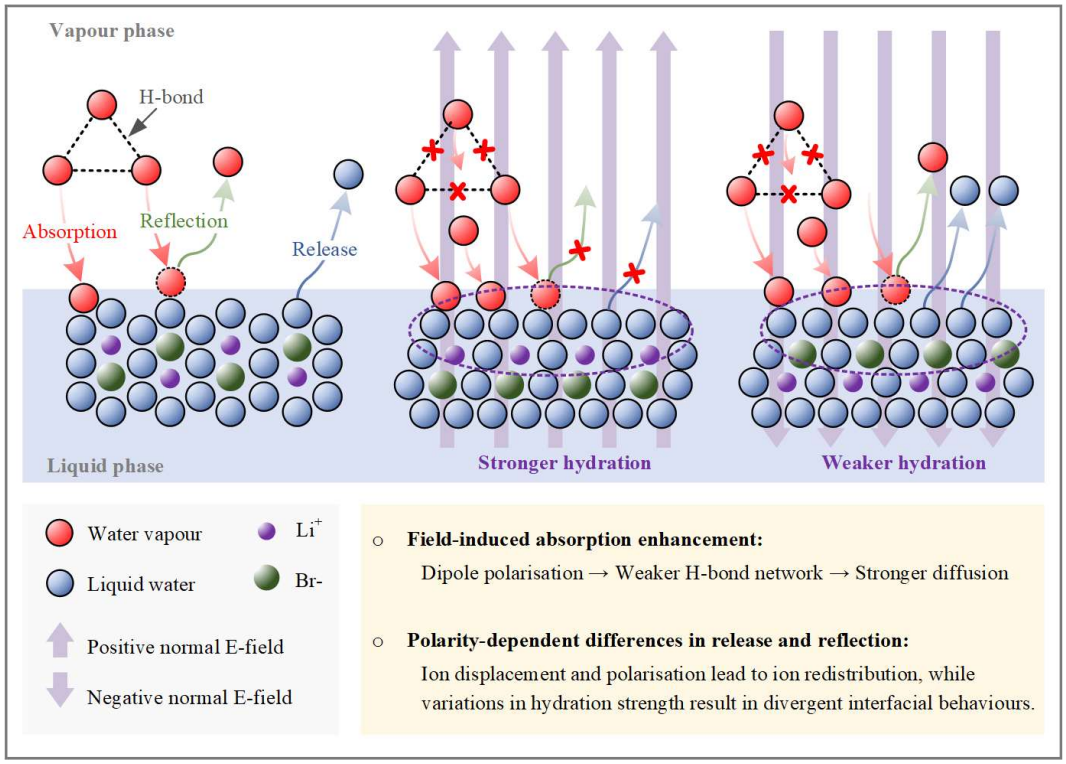


Fig. 12. Conceptual illustration of the regulation mechanism of interfacial molecular behaviours during the absorption process induced by *E*-field polarisation.

4. Conclusions

This work employed NEMD simulations to reveal the microscopic mechanisms by which perpendicular *E*-fields regulate water absorption at the vapour-liquid interface of concentrated LiBr solutions. Regardless of polarity, the *E*-field induced dipole reorientation, disrupting the H-bond network, accelerating network dissociation, and increasing molecular mobility, thereby enhancing interfacial diffusion. Diffusion coefficients increased by 22% and 9.6%, promoting spontaneous migration of water molecules from the vapour phase into the solution, resulting in net water absorption increases of 20% and 16%. System energy changes were negligible, ranging only from 0.18% to 0.6%. *E*-field polarity further modulated water release and reflection: under a positive field, interfacial Li^+ enrichment enhanced hydration and binding of water molecules, suppressing their release from the surface; under a negative field, Li^+

depletion and Br^- accumulation with weaker hydration facilitated water desorption. Polarity-dependent dipole reorientation induced by the *E*-field caused average dipole angles to decrease by 4.0° under the positive field and increase by 4.3° under the negative field, altering the relative positions of oxygen and hydrogen atoms at the interface and further modulating water release. Overall, the positive field produced a stronger enhancement than the negative field, indicating that *E*-field-induced polarisation, together with ion distribution and dipole orientation, can be harnessed to actively control interfacial mass transfer. These findings provide a theoretical basis for optimising liquid desiccant design and interfacial regulation strategies. The principles can also be extended to other gas-liquid absorption processes involving polar molecules, highlighting the broad potential for interfacial engineering applications.

Acknowledgments

We would like to acknowledge the Grant support from the National Natural Science Foundation of China (52476002)

References

[1] W. Shang, Z. Lv, Low carbon technology for carbon neutrality in sustainable cities: A survey, Sustain. Cities Soc. 92 (2023) 104489. https://doi.org/10.1016/j.scs.2023.104489.

[2] C. Che, Y. Yin, Improvement of low-grade heat utilization: Sensitivity mechanism of saturated vapor pressure-temperature in dehumidified materials, Applied Thermal Engineering 230 (2023) 120788. https://doi.org/10.1016/j.applthermaleng.2023.120788.

[3] J. Yu, Y. Xia, L. Chen, W. Yan, B. Liu, S. Jin, Full recovery of brines at normal temperature with process-heat-supplied coupled air-carried evaporating separation (ACES) cycle, Npj Clean Water 7 (2024) 133. https://doi.org/10.1038/s41545-024-00430-6.

[4] Z. Zhong, M. Burhan, K.C. Ng, X. Cui, Q. Chen, Low-temperature desalination

driven by waste heat of nuclear power plants: A thermo-economic analysis, Desalination 576 (2024) 117325. https://doi.org/10.1016/j.desal.2024.117325.

[5] Y. Li, Y. Xia, W. Deng, X. Gao, H. Li, X. Gao, Nucleate boiling heat transfer and critical heat flux in controllable droplet trains cooling, Appl. Therm. Eng. 267 (2025) 125824. https://doi.org/10.1016/j.applthermaleng.2025.125824.

[6] B. Yin, T. Ding, S. Wang, Z. Wang, B. Sun, W. Zhang, X. Zhang, Deformation and migration characteristics of bubbles moving in gas-liquid countercurrent flow in annulus, Petroleum Exploration and Development 52 (2025) 471-484. https://doi.org/10.1016/S1876-3804(25)60580-5.

[7] X. Gao, Y. Li, Y. Xia, H. Li, A REVIEW ON THERMO-FLUIDIC STUDY OF DROPLET IMPACT IN SPRAY COOLING, Heat Trans Res 56 (2025) 53-91. https://doi.org/10.1615/HeatTransRes.2024053386.

[8] C.-C. Yu, K.-Y. Chiang, A. Dhinojwala, M. Bonn, J. Hunger, Y. Nagata, Flipping Water Orientation at the Surface of Water-in-Salt and Salt-in-Water Solutions, J. Phys. Chem. Lett. 15 (2024) 10265-10271. https://doi.org/10.1021/acs.jpclett.4c01834.

[9] N. Habibollahi, A. Abdollahi, S.M. Sajadi, D. Toghraie, S. Emami, M. Shahgholi, M. Inc, Molecular dynamics simulation of combustion behavior of coated aluminum hydride nanoparticles in the oxygenated medium: Effects of adding the ethanol atomic coating, Eng. Anal. Bound. Elem. 150 (2023) 180-186. https://doi.org/10.1016/j.enganabound.2023.02.020.

[10] J. Tang, A. Ahmadi, A. Alizadeh, R. Abedinzadeh, A.M. Abed, G.F. Smaisim, S.K. Hadrawi, N. Nasajpour-Esfahani, D. Toghraie, Investigation of the mechanical properties of different amorphous composites using the molecular dynamics simulation, J. Mater. Res. Technol. 24 (2023) 1390-1400. https://doi.org/10.1016/j.jmrt.2023.02.193.

[11] Y. Zhou, E. Abdali, A. Shamshiri, M. Al-Bahrani, N. Sadoon, S. Ali Eftekhari, F.S. Hashim, N. Nasajpour-Esfahani, A.J. Khazel, L.Y. Qassem, D. Toghraie, The

computational study of initial temperature/pressure and atomic doping effects on the growth of crack in graphene nanostructure: Molecular dynamics approach, Mater. Sci. Eng. B 296 (2023) 116692. https://doi.org/10.1016/j.mseb.2023.116692.

[12] T. Chen, Y. Yin, Y. Zhang, X. Zhang, A molecular dynamics study on interaction contributions of components in liquid-vapor systems between LiBr aqueous solutions and air during absorption, Appl. Therm. Eng. 166 (2020) 114732. https://doi.org/10.1016/j.applthermaleng.2019.114732.

[13] Y. Pan, H. Liu, Z. Huang, W. Zhang, H. Gao, L. Liang, L. Dong, H. Meng, Membranes based on Covalent Organic Frameworks through Green and Scalable Interfacial Polymerization using Ionic Liquids for Antibiotic Desalination, Angew Chem Int Ed 63 (2024) e202316315. https://doi.org/10.1002/anie.202316315.

[14] L. Weng, W. Song, D.J. Jacobs, G.D. Elliott, Molecular insights into water vapor absorption by aqueous lithium bromide and lithium bromide/sodium formate solutions, Appl. Therm. Eng. 102 (2016) 125-133. https://doi.org/10.1016/j.applthermaleng.2016.03.153.

[15] Z. Zhong, Y. Ding, Y. Chen, P. Liao, Q. Chen, Improving commercial-scale alkaline water electrolysis systems for fluctuating renewable energy: Unsteady-state thermodynamic analysis and optimization, Appl. Energy 395 (2025) 126183. https://doi.org/10.1016/j.apenergy.2025.126183.

[16] A.M. Saitta, F. Saija, P.V. Giaquinta, Ab Initio Molecular Dynamics Study of Dissociation of Water under an Electric Field, Phys. Rev. Lett. 108 (2012) 207801. https://doi.org/10.1103/PhysRevLett.108.207801.

[17] W. Gao, H. Niu, T. Lin, X. Wang, L. Kong, Molecular dynamics study of response of liquid N,N-dimethylformamide to externally applied electric field using a polarizable force field, J. Chem. Phys. 140 (2014) 044501. https://doi.org/10.1063/1.4861893.

[18] C. Zhang, M. Sprik, Electromechanics of the liquid water vapour interface, Phys. Chem. Chem. Phys. 22 (2020), 10676-10686. https://doi.org/10.1039/c9cp06901a.

[19] F. S. Fan, Y. G. Yin, G. Y. Xu, B. J. Lei, W. H. Chen, Interfacial structure and transport properties of concentrated lithium chloride solutions under an electrostatic field, Colloid Surface A 685 (2024) 133217. https://doi.org/10.1016/j.colsurfa.2024.133217.

[20] B. B. Wang, X. D. Wang, Y. Y. Duan, M. Chen, Molecular dynamics simulation on evaporation of water and aqueous droplets in the presence of electric field, Int. J. Heat Mass Transfer 73 (2014) 533-541. https://doi.org/10.1016/j.ijheatmasstransfer.2014.02.034.

[21] J. Fei, B. Ding, S.W. Koh, J. Ge, X. Wang, L. Lee, Z. Sun, M. Yao, Y. Chen, H. Gao, H. Li, Mechanistic Investigation of Electrostatic Field-Enhanced Water Evaporation, Adv. Sci. 8 (2021) 2100875. https://doi.org/10.1002/advs.202100875.

[22] Y. Han, T. Zhang, X. Guo, T. Jiao, Insights into the mechanism of electrostatic field promoting ozone mass transfer in water: A molecular dynamics perspective, Sci. Total Environ. 848 (2022) 157710. https://doi.org/10.1016/j.scitotenv.2022.157710.

[23] H. Liu, J. Deng, H. Cai, B. Wang, Molecular dynamics study of the influence of electric fields on water penetration in metal confined nanochannels, J. Mol. Liq. 403 (2024) 124935. https://doi.org/10.1016/j.molliq.2024.124935.

[24] A.P. Thompson, H.M. Aktulga, R. Berger, D.S. Bolintineanu, W.M. Brown, P.S. Crozier, P.J. In ' T Veld, A. Kohlmeyer, S.G. Moore, T.D. Nguyen, R. Shan, M.J. Stevens, J. Tranchida, C. Trott, S.J. Plimpton, LAMMPS - a flexible simulation tool for particle-based materials modeling at the atomic, meso, and continuum scales, Comput. Phys. Commun. 271 (2022) 108171. https://doi.org/10.1016/j.cpc.2021.108171.

[25] X.H. Liu, K.Y. Qu, Y. Jiang, Empirical correlations to predict the performance of the dehumidifier using liquid desiccant in heat and mass transfer, Renew. Energy 31 (2006) 1627-1639. https://doi.org/10.1016/j.renene.2005.08.029.

[26] D.-M. Duh, D. Henderson, R.L. Rowley, Some effects of deviations from the

538 Lorentz-Berthelot combining rules for mixtures of Lennard-Jones fluids, Mol. Phys.
539 91 (1997) 1143-1147. https://doi.org/10.1080/002689797170879.

540 [27] S. Koneshan, J.C. Rasaiah, R.M. Lynden-Bell, S.H. Lee, Solvent Structure,
541 Dynamics, and Ion Mobility in Aqueous Solutions at 25 °C, J. Phys. Chem. B 102
542 (1998) 4193-4204. https://doi.org/10.1021/jp980642x.

543 [28] F.M. Mourits, F.H.A. Rummens, A critical evaluation of Lennard-Jones and
544 Stockmayer potential parameters and of some correlation methods, Can. J. Chem.
545 55 (1977) 3007-3020. https://doi.org/10.1139/v77-418.

546 [29] H.J.C. Berendsen, J.R. Grigera, T.P. Straatsma, The missing term in effective pair
547 potentials, J. Phys. Chem. 91 (1987) 6269-6271.
548 https://doi.org/10.1021/j100308a038.

549 [30] S. Miyamoto, P.A. Kollman, Settle: An analytical version of the SHAKE and
550 RATTLE algorithm for rigid water models, J Comput Chem 13 (1992) 952-962.
551 https://doi.org/10.1002/jcc.540130805.

552 [31] R.W. Hockney, R, Computer Simulation Using Particles, IOP Publishing, Bristol,
553 1988. https://doi.org/10.1201/9780367806934.

554 [32] N.S. Martys, R.D. Mountain, Velocity Verlet algorithm for dissipative-particle-
555 dynamics-based models of suspensions, Phys. Rev. E 59 (1999) 3733-3736.
556 https://doi.org/10.1103/PhysRevE.59.3733.

557 [33] F. Creazzo, S. Pezzotti, S. Bougueroua, A. Serva, J. Sponer, F. Saija, G. Cassone,
558 M.-P. Gaigeot, Enhanced conductivity of water at the electrified air-water interface:
559 a DFT-MD characterization, Phys. Chem. Chem. Phys. 22 (2020) 10438-10446.
560 https://doi.org/10.1039/C9CP06970D.

561 [34] T. Chen, Y. Yin, Y. Zhang, X. Zhang, Model evaluation of lithium bromide aqueous
562 solution and characteristics of water transport behaviors in liquid-vapor systems by
563 molecular dynamics, Int. J. Refrig. 107 (2019) 165-173.
564 https://doi.org/10.1016/j.ijrefrig.2019.08.001.

[35] P. Varilly, D. Chandler, Water Evaporation: A Transition Path Sampling Study, J. Phys. Chem. B 117 (2013) 1419-1428. https://doi.org/10.1021/jp310070y.

[36] E. Bird, J. Gutierrez Plascencia, P. Keblinski, Z. Liang, Molecular simulation of steady-state evaporation and condensation of water in air, Int. J. Heat Mass Transfer 184 (2022) 122285. https://doi.org/10.1016/j.ijheatmasstransfer.2021.122285.

[37] R.S. Taylor, L.X. Dang, B.C. Garrett, Molecular Dynamics Simulations of the Liquid/Vapor Interface of SPC/E Water, J. Phys. Chem. 100 (1996) 11720-11725. https://doi.org/10.1021/jp960615b.

[38] Z. Wang, D. Orejon, K. Sefiane, Y. Takata, Water vapor uptake into hygroscopic lithium bromide desiccant droplets: mechanisms of droplet growth and spreading, Phys. Chem. Chem. Phys. 21 (2019) 1046-1058. https://doi.org/10.1039/C8CP04504F.

[39] Z. Ying, L. YuLong, Nonequilibrium molecular dynamics simulations of mass transfer on transient direct-contact condensation, Int. J. Heat Mass Transfer 184 (2022) 122255. https://doi.org/10.1016/j.ijheatmasstransfer.2021.122255.

[40] T. Seki, C.-C. Yu, K.-Y. Chiang, A. Greco, X. Yu, F. Matsumura, M. Bonn, Y. Nagata, Ions Speciation at the Water-Air Interface, J. Am. Chem. Soc. 145 (2023) 10622-10630. https://doi.org/10.1021/jacs.3c00517.

[41] W.Q. Chen, M. Sedighi, F. Curvalle, A.P. Jivkov, Elevated temperature effects (T > 100 °C) on the interfacial water and microstructure swelling of Na-montmorillonite, Chem. Eng. J. 481 (2024) 148647. https://doi.org/10.1016/j.cej.2024.148647.

[42] H.H. Loeffler, B.M. Rode, The hydration structure of the lithium ion, J. Chem. Phys. 117 (2002) 110-117. https://doi.org/10.1063/1.1480875.

[43] H. Peng, M. Firouzi, Evaluation of interfacial properties of concentrated KCl solutions by molecular dynamics simulation, Colloid Surface A 538 (2018) 703-710. https://doi.org/10.1016/j.colsurfa.2017.11.063.

[44] D. Bratko, C.D. Daub, K. Leung, A. Luzar, Effect of Field Direction on

592 Electrowetting in a Nanopore, J. Am. Chem. Soc. 129 (2007) 2504-2510.
593 https://doi.org/10.1021/ja0659370.

594 [45] X. Wu, L. Lu, Y. Zhu, Y. Zhang, W. Cao, X. Lu, Ionic hydration of Na+ inside
595 carbon nanotubes, under electric fields, Fluid Ph. Equilib. 353 (2013) 1-6.
596 https://doi.org/10.1016/j.fluid.2013.06.001.

597 [46] J. Chanda, S. Bandyopadhyay, Hydrogen Bond Lifetime Dynamics at the Interface
598 of a Surfactant Monolayer, J. Phys. Chem. B 110 (2006) 23443-23449.
599 https://doi.org/10.1021/jp065203+.

600 [47] T. Chen, Y. Yin, P. Yan, Y. Ling, F. Wang, Y. Chen, Mechanism study on magnitude
601 of mass transfer coefficients in liquid desiccant dehumidification and regeneration,
602 Appl. Therm. Eng. 204 (2022) 117951.
603 https://doi.org/10.1016/j.applthermaleng.2021.117951.